

Concurrently enhanced piezoelectric performance and curie temperature in stressed lead-free $\text{Ba}_{0.85}\text{Ca}_{0.15}\text{Ti}_{0.9}\text{Zr}_{0.1}\text{O}_3$ ceramics

Received: 7 December 2024

Accepted: 16 April 2025

Published online: 30 April 2025

Yuanhui Su¹, Qingying Wang¹, Yu Huan¹✉, Jianli Wang², Wei Sun³, Yongjun Li⁴, Tao Wei¹✉ & Zhenxiang Cheng²✉

Eco-friendly, lead-free BaTiO_3 -based piezoelectrics are critical for sustainable electronics, but improving their piezoelectric properties often compromises Curie temperature (T_C). To address this trade-off, we implemented an innovative stress engineering approach by introducing a secondary phase BaAl_2O_4 in $\text{Ba}_{0.85}\text{Ca}_{0.15}\text{Ti}_{0.9}\text{Zr}_{0.1}\text{O}_3$ (BCTZ) ceramics. The thermal expansion mismatch between BCTZ and BaAl_2O_4 induces internal stress within the BCTZ matrix, causing significant lattice distortion and phase fraction modulation, which improves both T_C and the piezoelectric coefficient (d_{33}). Additionally, the local electric field and Al^{3+} doping in ABO_3 lattice further enhance d_{33} . Optimized BCTZ ceramics achieve d_{33} of $650 \pm 16 \text{ pC N}^{-1}$, d_{33}^* of 1070 pm V^{-1} , and T_C of $96.5 \pm 1.0^\circ\text{C}$, placing them at the forefront of lead-free BaTiO_3 -based piezoelectrics. This study underscores the effectiveness of bulk stress engineering via a secondary phase for enhancing lead-free piezoelectric ceramics, paving the way for developing high-performance piezoelectric ceramics suitable for broad temperature applications.

Over the past few decades, the piezoelectric materials market has predominately relied on lead-based piezoelectric ceramics. However, escalating environmental concerns have spurred extensive endeavors to explore lead-free alternatives. Among these, $\text{Ba}_{0.85}\text{Ca}_{0.15}\text{Ti}_{0.9}\text{Zr}_{0.1}\text{O}_3$ (BCTZ) ceramics have emerged as promising candidates due to their high piezoelectric coefficient ($d_{33} > 500 \text{ pC N}^{-1}$)^{1–3}, garnering widespread attention. Many efforts, such as optimizing sintering processes⁴, employing doping strategies^{5–7}, and incorporating second-phase materials⁸, have been carried out to further enhance the performance of BCTZ-based ceramics. Nevertheless, several challenges persist that hinder their practical application³. Specially, it is widely recognized that trade-offs among performance parameters exist in

most piezoelectric ceramics, making it difficult to achieve simultaneous improvement across multiple parameters, particularly the concurrent achievement of high Curie temperature (T_C) and high d_{33} . A primary concern is the relatively low T_C ($\sim 90^\circ\text{C}$) of BCTZ piezoelectric ceramics, which limits their operational temperature range. Notably, enhancing piezoelectricity often comes at the expense of T_C (Supplementary Fig. 1)^{7–13}, highlighting the necessity to improve both piezoelectric properties and T_C concurrently to broaden the applications of lead-free BCTZ-based piezoceramics.

Strain engineering of perovskite oxide thin films has emerged as an exceptionally powerful technique for manipulating ferroelectric behavior^{14–17}. Schlom et al. were the first to demonstrate that

¹School of Material Science and Engineering, University of Jinan, Jinan, China. ²Institute for Superconducting and Electronic Materials, Faculty of Engineering and Information Sciences, University of Wollongong Innovation Campus, North Wollongong, NSW, Australia. ³Shandong Provincial Key Laboratory of Preparation and Measurement of Building Materials, University of Jinan, Jinan, China. ⁴Bruker (Beijing) Scientific Technology Co. Ltd, Beijing, China.

✉ e-mail: mse_huany@ujn.edu.cn; mse_weit@ujn.edu.cn; cheng@uow.edu.au

introducing epitaxial strain and stress in SrTiO₃ films grown on perovskite-type substrate can improve the T_C by inducing lattice distortion, thereby stabilizing the ferroelectric phase¹⁸. Subsequently, various methods have been developed to modulate the in-plane strains of ferroelectric films, allowing for precise control over various properties such as crystal symmetry, domain structure, defect concentration, and phase ratio^{17,19,20}. Despite its effectiveness in tailoring the physical properties of ferroelectric films, the application of strain engineering in the field of piezoelectric ceramics remains largely unexplored.

Inspired by strain engineering in ferroelectric thin films, we present a novel stress engineering strategy aimed at simultaneously enhancing the T_C and d_{33} of BCTZ-based ceramics. Specifically, lead-free ceramics composed of Ba_{0.85}Ca_{0.15}Ti_{0.9}Zr_{0.1}O_{3-x} and a small amount of BaAl₂O₄ were fabricated through the doping of AlN particles. The underlying causes of the secondary phase with varying doping amounts and particle sizes on the piezoelectric performance and T_C are systematically investigated. Encouragingly, this approach yielded an ultrahigh piezoelectric property ($d_{33} = 650 \pm 16$ pC N⁻¹, $d_{33}^* = 1070$ pm V⁻¹) along with an excellent T_C (96.5 ± 1.0 °C). This study

provides an example of simultaneously elevating both the T_C and d_{33} of piezoelectric ceramics, offering a promising avenue for future research on high-performance lead-free piezoelectric ceramics.

Results

Piezo- and ferroelectric properties

Ba_{0.85}Ca_{0.15}Ti_{0.9}Zr_{0.1}O_{3-x} mol% AlN (50 nm) (BCTZ-*x*AlN-50, *x* = 0.25, 1.00, 1.50, and 1.75), Ba_{0.85}Ca_{0.15}Ti_{0.9}Zr_{0.1}O_{3-x} mol% AlN (300 nm) (BCTZ-*x*AlN-300, *x* = 0.25, 0.50, 0.75, 1.00, 1.25, 1.50, 1.75, and 2.00), and Ba_{0.85}Ca_{0.15}Ti_{0.9}Zr_{0.1}O_{3-x} mol% AlN (3000 nm) (BCTZ-*x*AlN-3000, *x* = 0.25, 1.00, 1.50, and 1.75) ceramics were prepared using AlN with sizes of 50 nm, 300 nm, and 3000 nm (Supplementary Fig. 2) by a conventional solid-state reaction method, respectively. The comparison of d_{33} and T_C of BCTZ-*x*AlN-50, BCTZ-*x*AlN-300, and BCTZ-*x*AlN-3000 ceramics is depicted in Fig. 1a. The T_C was determined by temperature dependence of dielectric constant (ϵ_r -*T*) and dielectric loss ($\tan\delta$ -*T*) curves illustrated in Supplementary Figs. 3–5. For BCTZ-*x*AlN-50, a significant reduction in T_C is observed, while d_{33} shows a slight improvement. For BCTZ-*x*AlN-300 ceramics, the d_{33} initially increases as the AlN doping concentration increases up

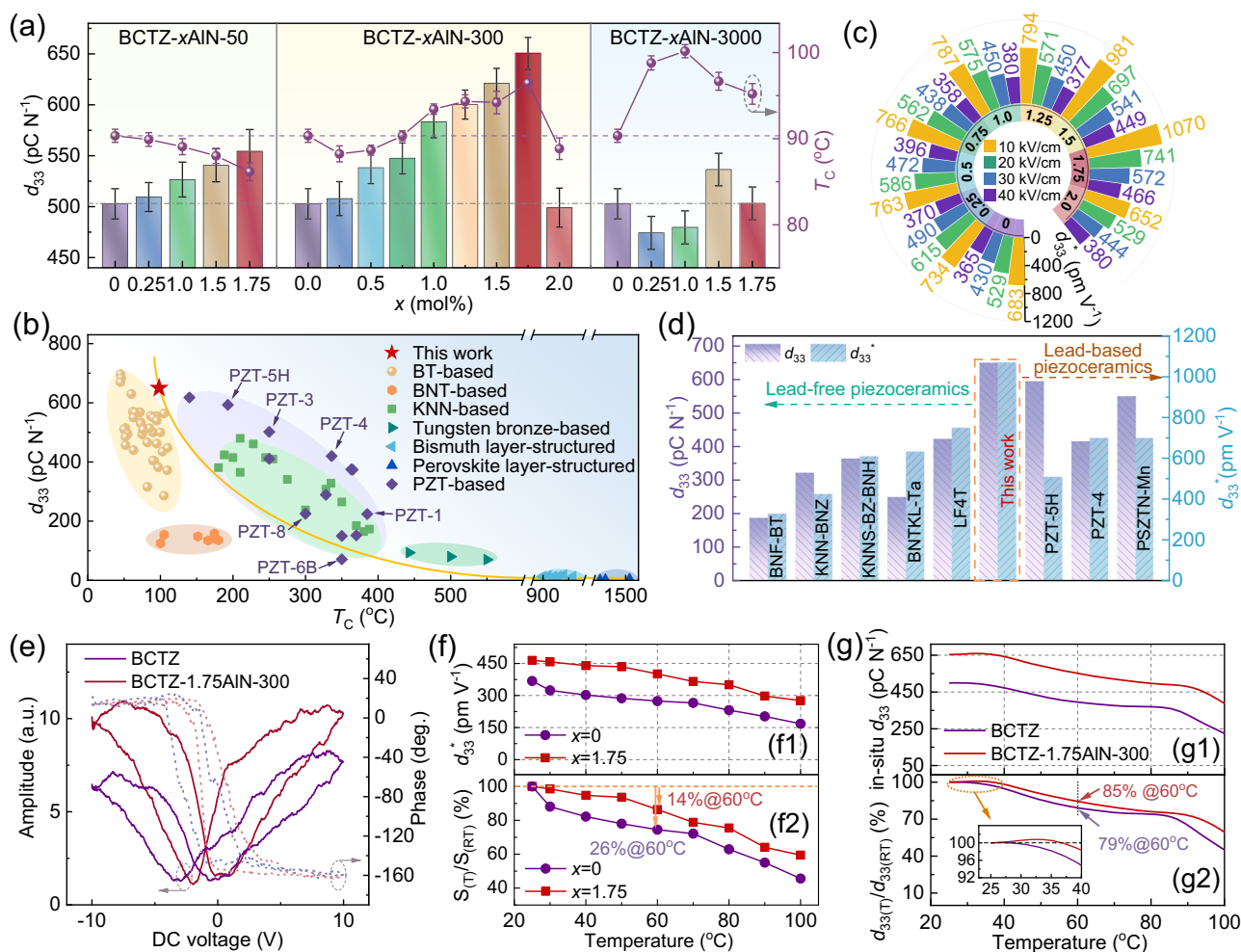


Fig. 1 | Piezo- and ferroelectric properties of BCTZ-*x*AlN-50 ceramics.

a Comparison of the d_{33} and T_C of BCTZ-*x*AlN-50 ceramics, BCTZ-*x*AlN-300 ceramics, and BCTZ-*x*AlN-3000 ceramics. Error bars show standard error of mean. **b** Comparison of d_{33} and T_C with the other piezoceramics^{37,21–27}. **c** The electric field dependent d_{33}^* for BCTZ-*x*AlN-300 ceramics. **d** Comparison of d_{33} and d_{33}^* with the other piezoceramics^{28–32}. **e** PFM amplitude and phase hysteresis versus voltage loops of BCTZ ceramic and BCTZ-1.75AlN-300 ceramic. **f1** Temperature-dependent d_{33} of BCTZ and BCTZ-1.75AlN-300 ceramics. **f2**

Comparison of the normalized d_{33} between BCTZ and BCTZ-1.75AlN-300 ceramics under different temperatures. Normalized d_{33} is defined as the ratio of the d_{33}^* value measured at various temperatures to the d_{33} value measured at the initial room temperature. **g1** The in-situ d_{33} as a function of temperature for BCTZ and BCTZ-1.75AlN-300 ceramics. **g2** Comparison of the normalized d_{33} between BCTZ and BCTZ-1.75AlN-300 ceramics at different temperatures. The inset is the enlarged view of the normalized d_{33} between 25 and 40 °C.

to 1.75 and then decreases beyond 1.75. Notably, the BCTZ–1.75AlN–300 ceramic achieves an ultrahigh d_{33} of $650 \pm 16 \text{ pC N}^{-1}$, which is $\sim 30\%$ higher than that of pure BCTZ ceramic ($503 \pm 15 \text{ pC N}^{-1}$). Meanwhile, the T_C of BCTZ– x AlN–300 ceramics initially decreases with the AlN doping concentration, declining from $90.2 \pm 0.8^\circ\text{C}$ in pure BCTZ to $88.2 \pm 0.9^\circ\text{C}$ in BCTZ–0.25AlN–300. Subsequently, as the doping concentration increases, T_C exhibits a rapid rise, reaching a maximum of $96.5 \pm 1.0^\circ\text{C}$ at $x = 1.75$. Remarkably, doping BCTZ ceramics with AlN can simultaneously improve both d_{33} and T_C , exceeding those of previously reported BaTiO₃-based lead-free piezoceramics, including BCTZ, BCTSn, and BCTHf-based compositions (summarized in Supplementary Fig. 6 and Supplementary Table 1; Supplementary Note 1). Our findings demonstrate significant progress in piezoelectric properties for BaTiO₃-based ceramics, alleviating the trade-off relationship between d_{33} and T_C , making them highly competitive to replace traditional lead-based materials (Fig. 1b)^{3,7,21–27}. Meanwhile, BCTZ– x AlN–3000 ceramics exhibit a significant increase in T_C accompanied by a slight suppression in d_{33} . These results imply that the incorporation of AlN, with varying dopant sizes and concentrations, exhibits significant influence on ceramic performance, and subsequent analysis will delve deeper into this impact.

The unipolar strain-electric field (S – E) curves of the BCTZ– x AlN–300 ceramics are presented in Supplementary Fig. 7. The converse piezoelectric coefficient ($d_{33}^* = S_{\text{max}}/E_{\text{max}}$, where S_{max} is the maximum strain and E_{max} is the maximum electric field) derived from the unipolar S – E curves at varied electric fields is detailed in Fig. 1c. The doping of AlN markedly improves the strain in the ceramics, with the most pronounced effect observed in the BCTZ–1.75AlN–300 ceramic. This particular ceramic achieves the highest $d_{33}^* = 1070 \text{ pm V}^{-1}$ at an electric field of 10 kV cm^{-1} , which is 0.6 times greater than that of the pure BCTZ ceramic (680 pm V^{-1}). Figure 1d compares the d_{33} and d_{33}^* values of lead-based and lead-free piezoelectric ceramics, indicating that the high-performance BCTZ–1.75AlN–300 ceramics in this work have greater potential for electro-mechanical conversion compared to other lead-based and lead-free piezoelectric ceramic systems^{28–32}. Specifically, when compared to traditional lead-based materials, such as PZT-5H, our BCTZ–1.75AlN–300 ceramics offer a balanced combination of high piezoelectric performance and moderate thermal stability. These properties showcase them promising potential as a viable alternative to lead-based ceramics. Notably, the local polarization-electric field hysteresis loops of BCZT and BCTZ–1.75AlN–300 ceramics were recorded by SS-PFM measurements, reflecting the local piezoelectric response (Fig. 1e). The phase hysteresis loops exhibit a characteristic 180° contrast, indicating a fully reversible polarization dynamic. The amplitude of both samples shows butterfly loops describing the local displacement as a function of voltage, which is typical of the piezoelectric response in ferroelectric materials. The BCTZ–1.75AlN–300 sample demonstrates an increased amplitude compared to the undoped BCZT ceramics, offering direct microscopic evidence of the significantly enhanced piezoelectric response in BCTZ–1.75AlN–300 ceramics. The polarization-electric field (P – E) loops of the BCTZ– x AlN–300 ceramics reveal that BCTZ–1.75AlN–300 ceramic exhibits both the largest maximum polarization (P_{max}) of $18.9 \mu\text{C cm}^{-2}$ and largest remnant polarization (P_r) of $9.54 \mu\text{C cm}^{-2}$ among all the ceramics (Supplementary Figs. 8–9, Supplementary Note 2). Additionally, the P – E and S – E curves for the BCTZ– x AlN–50 and BCTZ– x AlN–3000 ceramics are depicted in Supplementary Figs. 10–11, respectively. When compared to BCTZ– x AlN–300 samples with equivalent doping levels, both BCTZ– x AlN–50 and BCTZ– x AlN–3000 ceramics exhibit lower strain and polarization values. The d_{33}^* behavior of the BCTZ– x AlN–50 and BCTZ– x AlN–3000 ceramics corresponds to the changes in d_{33} observed in their respective ceramics. The optimal d_{33}^* values for BCTZ– x AlN–50 and BCTZ– x AlN–3000 ceramics are achieved at doping levels of $x = 1.75$ and $x = 2.00$, respectively, under an electric field of 10 kV cm^{-1} , with values of 860 and 902 pm V^{-1} , accordingly.

To evaluate the thermal stability of the ceramics, we measured the unipolar strain and in-situ d_{33} as a function of temperature. Temperature-dependent unipolar S – E curves of BCTZ and BCTZ–1.75AlN–300 ceramics are examined (Supplementary Fig. 12), and the corresponding d_{33}^* are summarized in Fig. 1f. As the temperature increases, the strain in BCTZ–1.75AlN–300 ceramics decreases slowly, with an overall variation of less than 14% over the temperature range from 25 to 60°C . The data obtained from multiple measurements of BCTZ–1.75AlN–300 ceramics demonstrates good repeatability (Supplementary Fig. 13). In contrast, the strain of BCTZ ceramics decreases sharply, exhibiting a larger variation of 26%. Additionally, the in-situ thermal stability of d_{33} from 25 to 100°C and the corresponding normalized d_{33} retention are shown in Fig. 1g. As the temperature increases, the d_{33} of BCTZ ceramic decreases monotonically, whereas the d_{33} of BCTZ–1.75AlN–300 ceramic initially increases and then decreases. At 60°C , the BCTZ–1.75AlN–300 ceramic exhibits a d_{33} of 550 pC N^{-1} and a d_{33} retention of 85%, which is higher than that of BCTZ ceramics and other AlN-doped BCTZ ceramics (Supplementary Fig. 14), demonstrating its strong potential for broad-temperature applications.

Additionally, the ε_r – T and $\tan\delta$ – T curves of BCTZ– x AlN–300 ceramics are measured to accurately determine the phase transformation temperatures (Supplementary Fig. 4). All ceramics exhibit three anomalies corresponding to the phase transitions from ferroelectric rhombohedral to orthorhombic ($T_{\text{R-O}}$), orthorhombic to tetragonal ($T_{\text{O-T}}$), and tetragonal to paraelectric cubic phases (T_C), which are summarized in Supplementary Fig. 15. The MPB at room temperature mitigates polarization anisotropy by facilitating polarization rotation between the tetragonal (001)_T and the rhombohedral (111)_R phase states, contributing to the outstanding piezoelectric and dielectric properties (Supplementary Fig. 16)^{33,34}.

Phase structure and micromorphology

The as-synthesized ceramics were characterized using high-resolution Synchrotron X-ray diffraction technique (SXRD), as illustrated in Supplementary Figs. 17–18. Taking BCTZ– x AlN–300 ceramics as examples, all samples exhibit a typical perovskite structure. A weak diffraction peak observed at 2θ angle of 10.74° corresponds to the (020) planes of BaAl₂O₄ with hexagonal symmetry and $P6322$ space group (JCPDS No.17-0306). The same phenomenon can also be observed in both BCTZ– x AlN–50 and BCTZ– x AlN–3000 ceramics. Despite the introduction AlN in the precursor of BCTZ, its inherent instability at high temperatures ($>800^\circ\text{C}$) leads to a reaction between AlN and BCTZ during high-temperature sintering, resulting in the formation of BaAl₂O₄ (Supplementary Fig. 19 and Supplementary Note 3). This indicates that the actual composition of the secondary phase in BCTZ– x AlN ceramics is BaAl₂O₄, and AlN in the BCTZ– x AlN ceramics is solely utilized for descriptive annotation.

The impact of secondary phase BaAl₂O₄ on the phase transformation of BCTZ– x AlN ceramics was investigated. Initially, Fig. 2a depicts the contour plots of the (110) and (111) diffraction peaks of BCTZ– x AlN–300 ceramic. It is evident that the (110) and (111) diffraction peaks of BCTZ– x AlN ceramics shift to higher degrees as the dopant AlN particles increase, indicating a gradual enhancement in the shrinkage of BCTZ lattice. Subsequently, Rietveld refinement was applied to the high-resolution SXRD patterns to accurately determine the crystal structure. BaTiO₃, with its tetragonal (T) phase characterized by $P4mm$ space group (JCPDS No.05-0626), the orthorhombic (O) phase by the $Amm2$ space group (JCPDS No.81-2200), and the rhombohedral (R) phase by the $R3m$ space group (JCPDS No.85-0368), was used as the initial structural model for these refinements (Supplementary Fig. 20). The refinement results confirmed that all ceramics exhibit a coexistence of R, O, and T phases. The phase fractions for all ceramics are summarized in Fig. 2b. As the AlN doping concentration increases, the fractions of T phase and O phase of BCTZ– x AlN–300

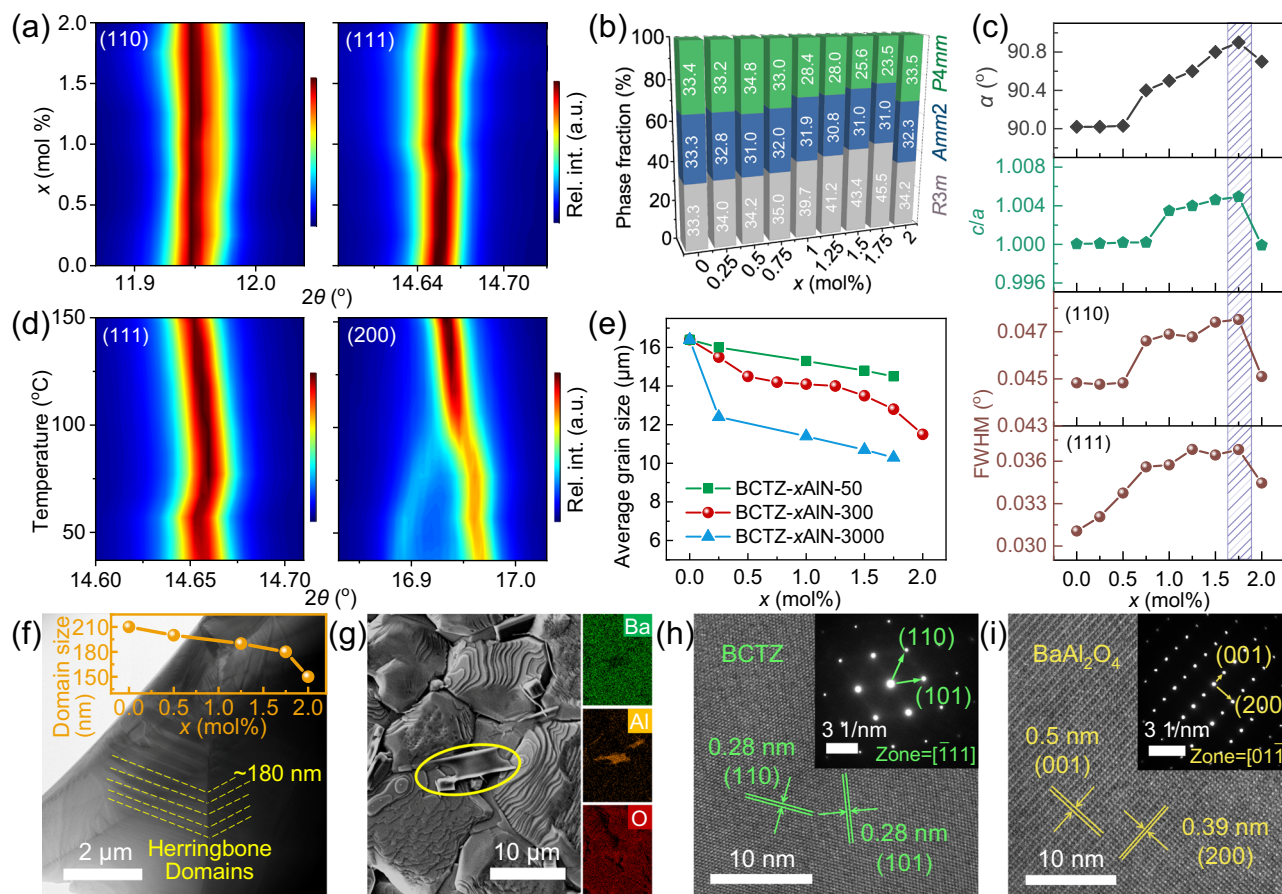


Fig. 2 | Phase and microstructure characterization of BCTZ-xAlN ceramics. **a** Evolution of (110) and (111) diffraction peaks as a function of the AlN doping content. **b** Phase fractions, **(c)** α angle of R phase, lattice constant (c/a) of T phase, and FWHM for the (110) and (111) planes of BCTZ-xAlN-300 ceramics obtained from the Rietveld refinement. **d** Contour plot of in-situ variable temperature SXRD for the (111) and (200) diffraction peaks of BCTZ-xAlN-300 ceramics. **e** Average

grain size of the BCTZ-xAlN ceramics. **f** TEM image of BCTZ-1.75AlN-300 ceramic (Inset is the average domain size of the BCTZ-xAlN ceramics). **g** SEM image and EDS mapping image of BCTZ-1.75AlN-300 ceramic (the yellow-circled area represents BaAl_2O_4). HRTEM images and corresponding SAED patterns of **(h)** BCTZ and **(i)** BaAl_2O_4 in BCTZ-1.75AlN-300 ceramics.

ceramics decrease initially, accompanied by a continuous increase in the R phase. Notably, BCTZ-1.75AlN-300 ceramics exhibit the highest fractions of R phase and the largest α angle, suggesting enhanced crystal asymmetry (Fig. 2c). Furthermore, this ceramic has the largest c/a ratio, indicating significant lattice distortion along the c -axis and substantial local displacement of B-site ions^{5,35}. Correspondingly, the full-width at half-maxima (FWHM) of (110) and (111) diffraction peaks in BCTZ-1.75AlN-300 ceramic, confirming maximal crystal asymmetry and lattice distortion⁷. These structural features contribute to an increased dipole moment, thereby enhancing piezoelectric performance (such as d_{33} and d_{33}^*).

Moreover, in-situ variable-temperature high-resolution SXRD has been utilized to investigate the crystallographic phase evolution of BCTZ-1.75AlN-300 ceramics (Supplementary Fig. 21). Contour maps of expanded SXRD patterns for the (111) and (200) diffraction peaks illustrate the temperature-induced phase transformations in BCTZ-1.75AlN-300 ceramics during heating process (Fig. 2d). Remarkably, the ceramics initially undergo a sequential disappearance of the R, O, and T phases upon heating, ultimately transforming into a paraelectric cubic (C) phase. This observation is consistent with the ε_r - T and $\tan\delta$ - T results. This phase transformation leads to a decrease in d_{33}^* and d_{33} as the temperature rises, as observed in Fig. 1f, g.

To further examine the local structure, the surface morphology and average grain size of thermally etched BCTZ-xAlN ceramics were analyzed using SEM (Supplementary Figs. 22–26). All ceramics exhibit

a highly dense microstructure, with a high relative density (above 95%) and low porosity (summarized in Supplementary Table 2 and Supplementary Note 4), which contributes to their electrical properties^{27,36}. The pristine BCTZ ceramic exhibits irregularly shaped grains with an average size of $\sim 16.4 \mu\text{m}$. The average grain size of BCTZ-xAlN-50, BCTZ-xAlN-300, and BCTZ-xAlN-3000 ceramics decreases markedly as AlN doping concentration increases (Fig. 2e). This continuous reduction in size can be attributed to the hindering effect of BaAl_2O_4 particles on the grain boundaries during the sintering process. The reduction in grain size leads to a refined domain configuration (Fig. 2f, Supplementary Fig. 27 and Supplementary Note 5). Specifically, the domain size decreases from 210 nm in the undoped BCTZ ceramic to 180 nm in the BCTZ-1.75AlN-300 sample. Considering that the domain size is proportional to the square root of the domain wall energy, this refinement facilitates the polarization orientation under an external electric field and the orderly arrangement of ferroelectric domains, thereby enhancing the extrinsic piezoelectric response of ceramics^{22,37,38}.

Energy dispersive X-ray spectroscopy (EDS) mapping further reveals the distinct distribution of the elements along grain boundaries in BCTZ-xAlN ceramics (Fig. 2g, Supplementary Figs. 28–30, and Supplementary Note 6). BCTZ-xAlN-50 ceramics exhibit nano-sized, plate-like BaAl_2O_4 particles that aggregate at the grain boundaries of the BCTZ matrix. In contrast, both BCTZ-xAlN-300 and BCTZ-xAlN-3000 ceramics feature BaAl_2O_4 particles with a micro-

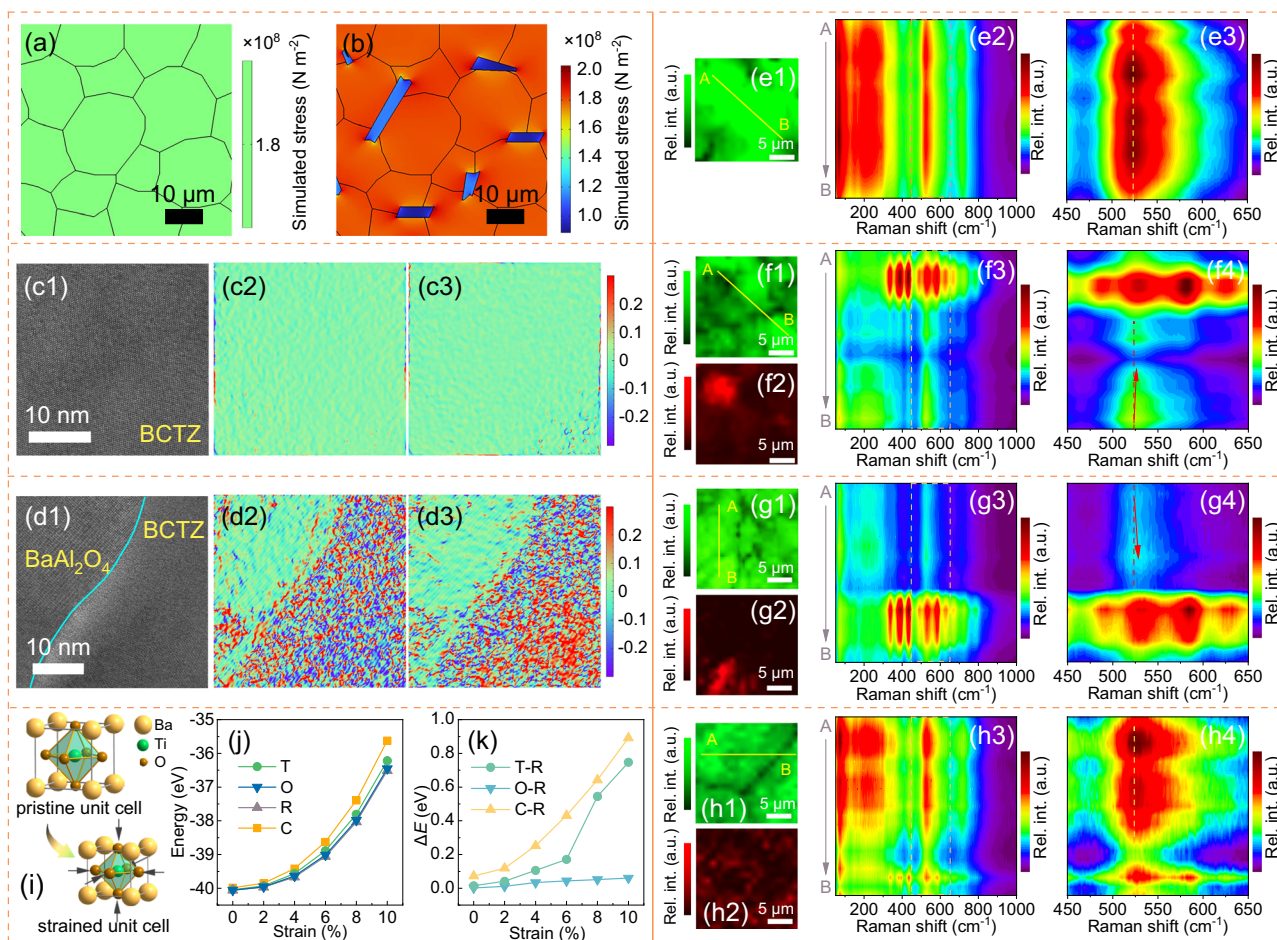


Fig. 3 | Stress in the BCTZ- x AlN ceramic. Finite-element simulation of internal stress distribution within (a) BCTZ and (b) BCTZ- x AlN ceramics. c1 HRTEM image of BCTZ and corresponding strain maps obtained by GPA along the (c2) xx direction and (c3) yy direction. d1 HRTEM image of BCTZ-1.75AlN-3000 and corresponding strain maps obtained by GPA along the (d2) xx direction and (d3) yy direction. Raman mapping images of ceramic integrating with the bands of 523 cm^{-1} : (e1) BCTZ, (f1) BCTZ-1.75AlN-300, (g1) BCTZ-1.75AlN-3000, and (h1) BCTZ-1.75AlN-50 ceramics. Raman mapping images of ceramic integrating with the bands of 390 cm^{-1} : (f2) BCTZ-1.75AlN-300, (g2) BCTZ-1.75AlN-3000, and

(h2) BCTZ-1.75AlN-50 ceramics. Corresponding contour plots of specific Raman spectra from points A to B in the bands range of 100–1000 cm^{-1} and 450–650 cm^{-1} , respectively: (e2–e3) BCTZ, (f3–f4) BCTZ-1.75AlN-300, (g3–g4) BCTZ-1.75AlN-3000, and (h3–h4) BCTZ-1.75AlN-50 ceramics. i Schematic of unit cell of pristine and strained BaTiO_3 bulk with (1×1) periodicities. j The total energies of the R, O, T, and C phases of BaTiO_3 as a function of strain. k The difference in the total energies of O, T, and C phases of BaTiO_3 and its R phase as a function of strain.

sized, strip-like shape. The average grain size distribution of these particles is summarized in the Supplementary Fig. 31. As the doping concentration increases or the average size of the AlN dopant particles increases, the average sizes of the BaAl_2O_4 secondary phase particles gradually increase. For example, at a doping concentration of $x = 1.75$, the grain size of BaAl_2O_4 in BCTZ-1.75AlN-3000 ceramic is 17 μm , which is larger than the 9 μm observed in BCTZ-1.75AlN-300 ceramic.

Scanning transmission electron microscopy (STEM) and the corresponding EDS elemental mapping of BCTZ-1.75AlN-300 ceramic were performed, with the results shown in Supplementary Fig. 32. The distribution of O and Ba elements appears uniform throughout the mapping area, whereas Al elements are predominantly concentrated in the central region. This concentration suggests the presence of two distinct co-existing phases. Furthermore, the high-resolution TEM (HRTEM) image of the BCTZ-1.75AlN-300 ceramics reveals two different sets of lattice fringes (Fig. 2h–i). The interplanar spacings of 0.28 nm correspond to both the (110) and (101) crystal planes of BCTZ, while those of 0.51 nm and 0.39 nm are associated with the (001) and (200) crystallographic planes of BaAl_2O_4 , respectively. The corresponding selected area electron diffraction (SAED) patterns, recorded along the $[\bar{1}11]$ and $[01\bar{1}]$ directions, respectively, provide further

confirmation of the high crystallinity of both BCTZ and BaAl_2O_4 phases.

Stress analysis

During the cooling stage of ceramic sintering, the disparity in thermal expansion coefficients between BCTZ ($-11.3 \times 10^{-6} \text{K}^{-1}$) and BaAl_2O_4 ($-5.8 \times 10^{-6} \text{K}^{-1}$) induces stress within the grains of BCTZ (Supplementary Fig. 33, Supplementary Note 7)^{14,39}. This stress plays a crucial role in determining the properties of ceramics. The stress distribution within BCTZ and BCTZ- x AlN ceramics was simulated by solving solid mechanics equilibrium conditions based on a finite element method using COMSOL Multiphysics® Software, as depicted in Fig. 3a, b. The irregular particles represent BCTZ, while the strip-like particles correspond to BaAl_2O_4 . In the BCTZ ceramics, no significant concentration of internal stress is observed across the grains. In contrast, the BCTZ- x AlN ceramics exhibit a pronounced heterogeneous stress distribution concentrated within the BCTZ grains, whereas the stress within the BaAl_2O_4 particles remains relatively low.

The heterogeneous stress within the BCTZ grains can lead to lattice strains. The geometric phase analysis (GPA) method was conducted to determine the internal stress in the selected areas of HRTEM

images of BCTZ and BCTZ-1.75AlN-300 (Fig. 3c, d). Both the unstressed BCTZ and the stressed BCTZ-1.75AlN-300 ceramics could be clearly observed in in-plane (ε_{xx}) and out-of-plane (ε_{yy}) strain maps. The BCTZ ceramic exhibited no obvious lattice distortion and strain within the grain. In contrast, GPA analysis at the interface of BCTZ-1.75AlN-300 ceramics reveals a substantial distribution of internal strain within the BCTZ region. These images provide direct evidence of the presence of secondary-phase-induced stress in BCTZ-1.75AlN-300 ceramics.

Moreover, Raman mapping spectra were collected at various spatial positions across the surface of BCTZ and BCTZ- x AlN ceramics to visually characterize the effect of internal stress on these ceramics. For both BCTZ and BCTZ- x AlN ceramics, the modes at 150 and 210 cm^{-1} , attributed to $A_1(\text{TO})$, are the characteristics of the R phase of BaTiO_3 ⁴⁰. The modes at 290 cm^{-1} , assigned to $E(\text{TO} + \text{LO})$, along with those at 450 cm^{-1} , serves as indicators of the O phase⁴¹. The modes at 350, 523, and 720 cm^{-1} correspond to $B_1(\text{TO})/E(\text{TO} + \text{LO})$, $E(\text{TO})/A_1(\text{TO})$, and $A_1(\text{LO})/E(\text{LO})$, respectively, representing the distinctive characteristics of the T phase^{6,41}. These Raman spectroscopy results indicate that both BCTZ and BCTZ- x AlN ceramics exhibit multi-phase coexistence, which is consistent with the observations from the SXRD, ε_r - T and $\tan\delta$ - T . Figure 3eI presents a color-coded Raman map that depicts the intensity around 523 cm^{-1} within a $20 \times 20 \mu\text{m}^2$ region of the BCTZ ceramic. Specific Raman spectra and the corresponding contour map from points A to B are detailed in the Supplementary Fig. 34 and Fig. 3e2-e3. Although there is a slight variation in peak intensity for BCTZ at all selected points, the positions of the peaks remain largely unchanged. This indicates a uniform distribution of stress within BCTZ ceramic, without any significant stress concentrations.

For the BCTZ-1.75AlN-300 ceramics, an additional Raman map depicting intensity around 430 cm^{-1} was collected (Fig. 3f and Supplementary Fig. 35). The peaks at 244 cm^{-1} , 430 cm^{-1} , 580 cm^{-1} , 670 cm^{-1} , and 780 cm^{-1} correspond to the $F_{2g}(1)$, E_g , $F_{2g}(2)$, $F_{2g}(3)$, and A_{1g} modes, respectively, indicative of BaAl_2O_4 ⁴². By utilizing the characteristic modes of both BCTZ and BaAl_2O_4 , we identified a single BaAl_2O_4 grain and two BCTZ grains along trajectory from point A to B. Changes induced by stress changes in the lattice of ceramic can affect the vibrational frequencies of phonon modes, leading to shifts in vibrational modes^{43,44}. The $E(\text{TO})/A_1(\text{TO})$ mode at -523 cm^{-1} is used to characterize the stress due to its relatively high intensity in all Raman spectra. Notably, for BCTZ-1.75AlN-300 ceramic, there is a noticeable shift in the peak positions of the mode at -523 cm^{-1} (indicated by red arrow), indicating the presence of stress within the BCTZ particles. Similarly, noticeable peak shift in the BCTZ-1.75AlN-3000 sample (marked by the red arrow) also indicates stress within the BCTZ particles due to micro-sized BaAl_2O_4 second phase (Fig. 3g and Supplementary Fig. 36). This stress is particularly prominent in samples with larger AlN particle sizes, where the formation of the secondary phase is more pronounced, contributing to substantial stress within the BCTZ matrix. This stress distorts the perovskite structure and significantly alters the lattice distortion in the ROT phases, thereby enhancing the T_C of the ceramic. It also modifies the phase fractions of the ROT phases, improving the piezoelectric response. Consequently, both T_C and the piezoelectric response are simultaneously enhanced in the ceramics, consistent with observations of T_C enhancement in stressed ferroelectric thin films^{18,20}. Conversely, due to nano-sized BaAl_2O_4 second phase, BCTZ-1.75AlN-50 ceramic exhibits relatively uniform unstressed BCTZ particles with no significant shift in the peak positions (Fig. 3h and Supplementary Fig. 37).

To further elucidate the effects of strain on BCTZ ceramics, we employed first-principles calculations within DFT to assess its influence on phase structural stability. Using BaTiO_3 as a representative model, different strain (0% to 10%) were applied to the unit cell (Fig. 3i). We calculated the total energies of the R, O, T, and paraelectric C phases of BaTiO_3 , with higher total energy indicating lower stability

(Fig. 3j). The results show that with 0–10% strain, the R phase consistently has the lowest total energy and highest stability, followed by the T phase, then the O phase, with the C phase being the least stable. The energy differences (ΔE) between the O, T, C phases and the R phase increase with strain, highlighting the higher stability of the R phase under stress compared to the other phases (Fig. 3k). This finding aligns well with experimental observations in BCTZ- x AlN-300 ceramics with $x < 1.75$. An increase in stress correlates with a gradual increase in the R phase content, a slight decrease in the O phase content, and a reduction in the T phase content, indicating that strain contributes to the enhanced piezoelectric response. Notably, the C phase is the most destabilized under strain, suggesting that strain inhibits the C phase's increase due to temperature rise, thereby improving the ceramic's temperature stability.

Local electric field and defect configuration

To further investigate the impact of the secondary phase BaAl_2O_4 on BCTZ- x AlN ceramics, a spatially resolved analysis of surface potential was conducted using KPFM to assess the local contact potential difference within the BCTZ-1.75AlN-300 ceramic. The contact potential difference (V_{CPD}) quantifies the variation in work functions between the AFM tip (W_{tip}) and the sample surface (W_{sample}), which can be expressed by the following equation:

$$V_{\text{CPD}} = \frac{W_{\text{tip}} - W_{\text{sample}}}{e} \quad (1)$$

Where e is the elementary charge. Examination of the topography of the BCTZ-1.75AlN-300 ceramic, as depicted in Fig. 4a, reveals a single BaAl_2O_4 grain situated at the boundary of BCTZ grain. The corresponding surface potential map, illustrated in Fig. 4b, highlights the potential contrast between the BaAl_2O_4 and BCTZ grains, with the BaAl_2O_4 exhibiting a higher surface potential characterized by a smaller work function. The potential profile illustrates a local potential difference of -65 mV between the BCTZ matrix and the BaAl_2O_4 , as evident from the potential *versus* distance curve (Fig. 4c). This observed potential disparity induces a local electric field at the interface of BCTZ and BaAl_2O_4 . However, this phenomenon is not observed in BCTZ ceramic (Supplementary Fig. 38, Supplementary Note 8). Notably, in the P - E loops of the AlN-doped BCTZ ceramics, the enhanced asymmetric characterization of the coercive electric field also confirms the presence of an internal electric field (Supplementary Fig. 39 and Supplementary Note 9). This internal electric field potentially leads to subtle structural distortion in BCTZ, further influencing the phase structure of ceramic^{45–47} and stabilizing the local ordering of ferroelectric domains⁴⁸. These effects enhance the piezoelectric response of BCTZ- x AlN ceramics.

To investigate the chemical states of the BCTZ- x AlN ceramics, the O elements in all BCTZ- x AlN-300 ceramics were examined using XPS spectra (Fig. 4d and Supplementary Fig. 40). The spectra can be fitted with four distinct peaks at binding energy of 529.0, 530.5, 531.5 and 532.5 eV, assigned to lattice oxygen (O1), highly oxidative oxygen species closely related to the surface oxygen vacancies (O2), the hydroxyl groups or the surface adsorbed oxygen (O3), and adsorbed molecular water (O4), respectively^{49–52}. The relative concentration of surface oxygen vacancies was estimated from the ratio (O2/O1) of oxygen species related to surface oxygen vacancies to lattice oxygen species⁵¹. It is observed that the oxygen vacancies concentration in BCTZ- x AlN-300 ceramics initially decreases and then increases with increasing x , reaching a minimum at $x = 1.75$ (Fig. 4e). These oxygen vacancies concentration change may be related to the incorporation of Al^{3+} into the lattice of BCTZ.

Initially, the formation of oxygen vacancies in all ceramics can be attributed to oxygen evaporation during the high-temperature

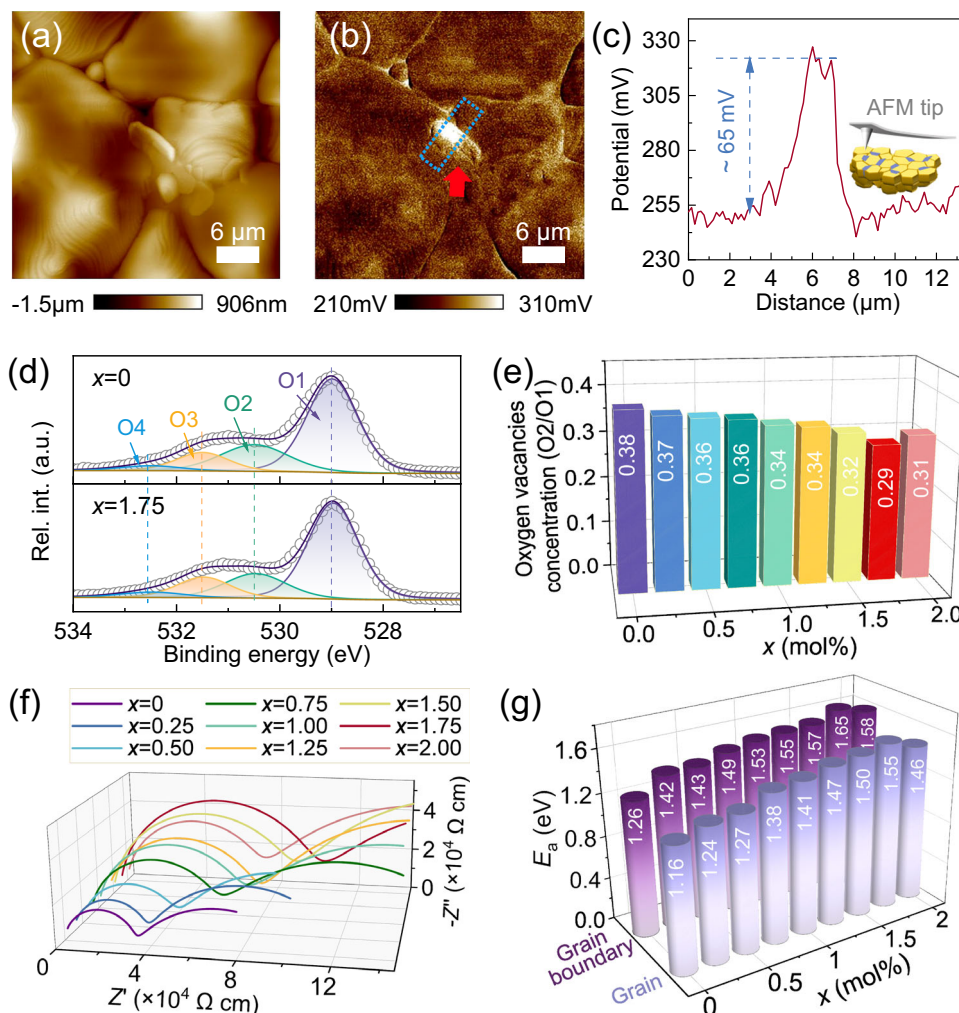
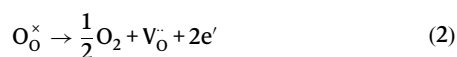


Fig. 4 | Local electric field and defect configuration of ceramics.

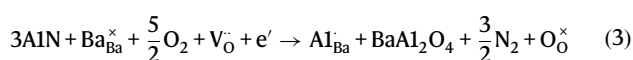
a Topographies, and **(b)** surface potential mapping of BCTZ-1.75AlN-300 ceramics measured using KPFM. **c** Surface potential profiles along the long edge of the region defined by the blue dashed box, as derived from the surface potential mappings. Inset is the schematic diagram of the KPFM testing. **d** XPS spectra of O1s

in BCTZ and BCTZ-1.75AlN-300 ceramics. **e** The concentration of oxygen vacancies (O2/O1 ratios). **f** Impedance spectra of BCTZ, BCTZ-*x*AlN-300 ceramics at 500 °C. **g** Fitted E_a values of grains and grain boundaries in BCTZ-*x*AlN-300 ceramics.

sintering process, which can be described by the following reaction.



In ceramics, two types of charge carriers can be generated: oxygen vacancies (V_0^{\cdot}) and free electrons (e^{\cdot}). For BCTZ-*x*AlN-300 ceramics with *x* ranging from 0.25 to 2.00, AlN doping leads to incorporation of Al^{3+} into the lattice, occupying A-sites in the perovskite structure and forming the extrinsic defect $\text{Al}_{\text{Ba,Ca}}^{\cdot}$. This incorporation alters the phase structure of the ceramics, enhancing the piezoelectric properties but also causing a decrease in the T_c of the ceramics. Simultaneously, the oxygen vacancies concentration in the ceramics is significantly reduced. The corresponding defect chemical equation is as follows.



Hence, the BCTZ-1.75AlN-300 ceramic exhibits a significantly reducing oxygen vacancies concentration, which also contributes to the enhanced resistivity of ceramics. This is verified by the impedance

spectra (Fig. 4f and Supplementary Fig. 41). Furthermore, these impedance spectra are fitted to evaluate the electrical microstructure of ceramics (Fig. 4g, Supplementary Figs. 42–43, and Supplementary Note 10). For all ceramics, the activation energy (E_a) at the grain boundaries is higher than within the grains, indicating that oxygen vacancies migration is more difficult at the grain boundaries. As AlN doping concentration increases, the E_a for both grains and grain boundaries in BCTZ-*x*AlN-300 ceramics increases significantly, indicating oxygen vacancy migration suppression. Notably, the BCTZ-1.75AlN-300 ceramic exhibits the highest E_a for both grains and grain boundaries, contributing to its exceptionally high piezoelectric performance.

Discussion

In this study, we investigated the influence of AlN with varying particle sizes and doping concentrations on BCTZ-based ceramics. The addition of AlN led to the formation of BaAl_2O_4 secondary phases and incorporation of Al^{3+} into lattice (Fig. 5a). Specifically, the reaction between AlN and BCTZ resulted in BaAl_2O_4 particles forming at the BCTZ grain boundaries, increasing stress within the BCTZ grain (stress effect, Fig. 5b). This stress caused lattice distortion and altered the phase fractions, resulting in simultaneous increases in

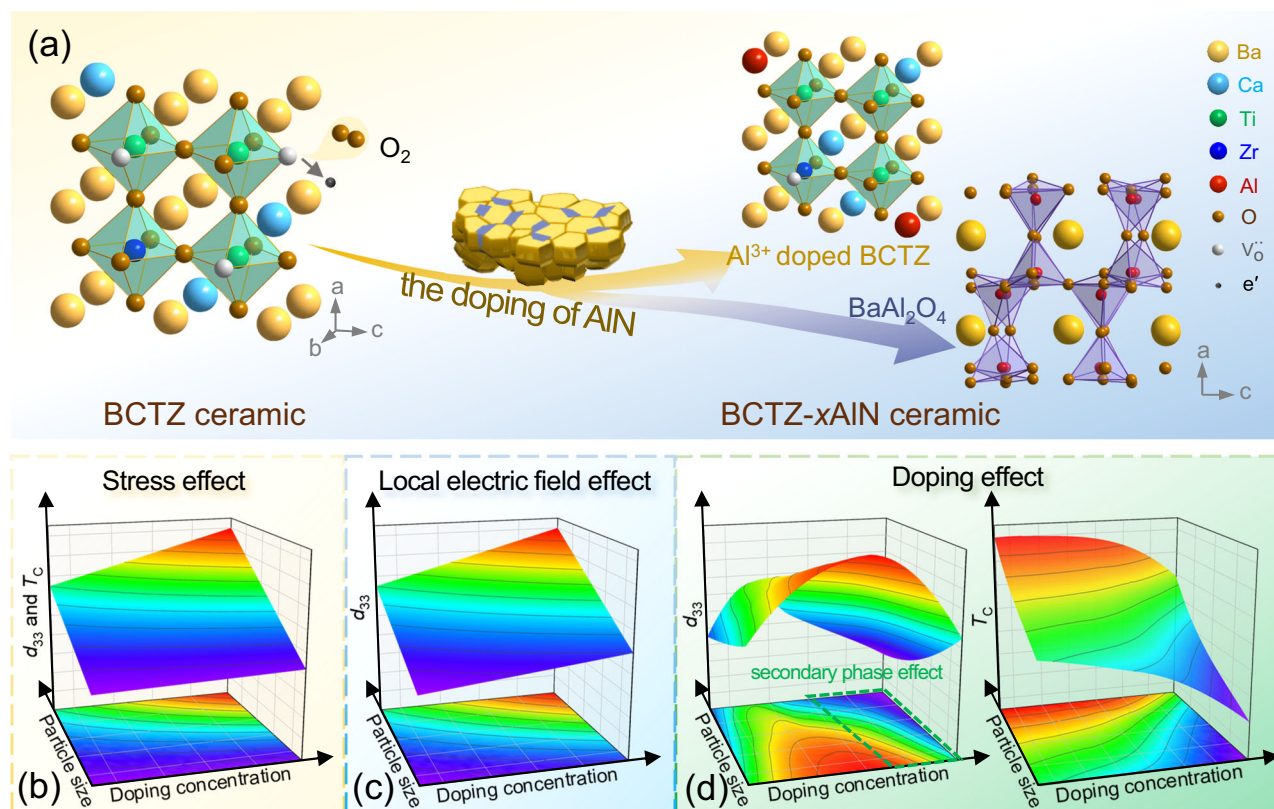


Fig. 5 | Schematic illustration for stress, local electric field, and doping effects. a Schematic illustration of AlN doped BCTZ-xAlN ceramics. Schematic illustration of the influence of (b) stress, (c) local electric field, and (d) doping effects on the

performance of ceramics as functions of AlN doping concentration and particle size. The z-axis indicates performance parameters such as d_{33} or T_C , where red represents higher values and purple indicates lower values.

both T_C and d_{33} . Additionally, the local electric field at BCTZ and BaAl₂O₄ interface enhanced d_{33} (local electric field effect, Fig. 5c). A small amount of Al³⁺ ions was incorporated into the A-sites of the perovskite lattice (doping effect, Fig. 5d), further modifying the phase structure and improving d_{33} but often reducing T_C . Both the AlN doping levels (mole ratio) and particle size (reaction activities) generated different stress, local electric field, and doping effects, and thus significantly influencing piezoelectric properties and T_C of the ceramics.

In the BCTZ-xAlN-3000 ceramics, as the AlN doping concentration increased, d_{33} initially decreased, then increased, and finally decreased again, while T_C initially rose and subsequently declined (Fig. 1a). For these ceramics, the secondary phase size reached the micrometer scale and significantly increased with higher doping levels, exceeding the dimensions of secondary phases in the BCTZ-xAlN-50 and BCTZ-xAlN-300 samples at the same doping concentrations. This negatively affected the piezoelectric performance of the ceramics. Additionally, the low reactivity of these large particles limited Al³⁺ doping effect, moderating the improvement in d_{33} . At lower doping levels, a substantial amount of the secondary phase formed with minimal Al³⁺ incorporation, leading to a significant rise in T_C due to the dominated stress effect. However, the excessive formation of large BaAl₂O₄ particles inhibited the increase in d_{33} . With further increases in doping concentration ($x=1.00$), a slight enhancement in d_{33} was observed, albeit accompanied by a minor decline in T_C , attributed to the moderate doping effect. At $x=1.75$, the doping effect contributed to an increase in d_{33} that was insufficient to offset the negative impacts of the excessive BaAl₂O₄ formation, resulting in decreases in both d_{33} and T_C .

Conversely, in BCTZ-1.75AlN-50 ceramics, the introduction of highly reactive nanoscale AlN promotes greater Al³⁺ doping, leading to a significant enhancement of d_{33} . However, this is accompanied by a

reduction in T_C due to insufficient stress generation. Thus, with increasing doping concentrations, the d_{33} of BCTZ-xAlN-50 ceramics increases while the T_C decreases. These contrasting behaviors reveal a crucial aspect: smaller AlN particles tend to be overly reactive, while larger particles are less reactive, resulting in either excessive or insufficient doping effect, respectively. Similarly, lower doping levels lead to inadequate doping and stress effects, while higher doping levels cause excessive doping and stress.

Encouragingly, the high-performance observed in BCTZ-xAlN-300 ceramics can be attributed to an optimal balance between the size of the secondary phase and the incorporation of Al³⁺ into the lattice. As the doping levels increased, d_{33} initially rose, reaching a maximum at $x=1.75$, before declining (Fig. 1a). Meanwhile, T_C exhibited a slight decrease at lower doping levels, followed by an increase peak at $x=1.75$, and a subsequent decrease. At low doping levels, the doping effect predominantly dictated the performance. As the doping concentration further increased, the combined effects of stress, electric field, and doping contributed to the overall enhancement of performance. The use of 300 nm AlN powder at a concentration of 1.75 mol% provided the most favorable conditions for enhancing the properties of the ceramics. Moderate particle size generated sufficient stress to enhance T_C , while still allowing controlled Al³⁺ doping, resulting in a simultaneous improvement in both T_C and d_{33} . However, this performance optimization was not without limitations. For BCTZ-2.00AlN-300 ceramics, excessive doping led to a reduction in lattice distortion, consequently diminishing d_{33} . The stress effect insufficiently counteracts the negative impacts of excessive doping effect, resulting in a significant reduction in T_C .

Through optimizing stress, local electric field, and doping effects, the highest piezoelectric properties ($d_{33}=650 \pm 16$ pC N⁻¹, $d_{33}^*=1070$ pm V⁻¹), a high T_C (96.5 ± 1.0 °C), and remarkable temperature stability, are achieved in BCTZ-1.75AlN-300. Our findings

elucidate the mechanisms behind the exceptional piezoelectric properties and desirable T_C of the BCTZ- x AlN ceramics, underscoring the effectiveness of bulk stress engineering through the introduction of a secondary phase in enhancing lead-free piezoelectric ceramics. This approach paves the way for developing high-performance piezoelectric materials suitable for a wide range of temperature applications.

Methods

Materials

Barium carbonate (BaCO_3 , 99%), calcium carbonate (CaCO_3 , 99%), and aluminum nitride with three different kinds of average sizes (AlN, 50 nm/300 nm/3000 nm, 99%) were purchased from Shanghai Macklin Biochemical Co, Ltd. Barium zirconium oxide (BaZrO_3 , 99%) was purchased from Alfa Aesar Co, Ltd. Titanium dioxide (TiO_2 , 99%) was purchased from Tianjin Fuchen Chemical reagents Co, Ltd. All the chemicals were used as received without further purification.

Preparation of ceramics

$\text{Ba}_{0.85}\text{Ca}_{0.15}\text{Ti}_{0.9}\text{Zr}_{0.1}\text{O}_3-x$ mol% AlN (300 nm) (BCTZ- x AlN-300, $x=0, 0.25, 0.50, 0.75, 1.00, 1.25, 1.50, 1.75$, and 2.00) ceramics were prepared by a conventional solid-state reaction method. The raw materials (BaCO_3 , CaCO_3 , BaZrO_3 , and TiO_2) were weighed according to stoichiometric ratios and ball-milled in ethanol for 12 h. The slurry was dried at 75°C and then calcined at 1150°C for 3 h, yielding single-phase BCTZ powders. Afterwards, both the BCTZ powders and the commercial AlN nanoparticles with the average size of 300 nm were weighed according to the formula of BCTZ- x AlN-300 ($x=0, 0.25, 0.50, 0.75, 1.00, 1.25, 1.50, 1.75$, and 2.00). Each mixture was ball-milled again in ethanol for 12 h and dried at 75°C . All specimens were pressed into disks with a diameter of 10 mm under 10 MPa and sintered at $1400\text{--}1450^\circ\text{C}$ for 3 h in air. The heating rate was 3°C min^{-1} and cooling rate was 1°C min^{-1} (sintering temperatures are summarized in Supplementary Table 2). Similarly, $\text{Ba}_{0.85}\text{Ca}_{0.15}\text{Ti}_{0.9}\text{Zr}_{0.1}\text{O}_3-x$ mol% AlN (50 nm) (BCTZ- x AlN-50, $x=0.25, 1.00, 1.50$, and 1.75) and $\text{Ba}_{0.85}\text{Ca}_{0.15}\text{Ti}_{0.9}\text{Zr}_{0.1}\text{O}_3-x$ mol% AlN (3000 nm) (BCTZ- x AlN-3000, $x=0.25, 1.00, 1.50$, and 1.75) were prepared using AlN nanoparticles with sizes of 50 nm and 3000 nm, respectively, following the same method.

Characterization

High-resolution synchrotron X-ray diffraction (SXRD) and in-situ variable temperature SXRD measurements were performed at the Powder Diffraction beamline of the Australian Synchrotron, using a wavelength of 0.590246 \AA and a scan speed of $0.2256^\circ\text{ min}^{-1}$. The crystal structures and lattice parameters of the ceramics were analyzed using GSAS-EXPGUI Rietveld refinement software^{53–55}. Scanning electron microscopy (SEM) images and EDS mapping were obtained using a field emission SEM (Gemini 300, Zeiss, Germany). Transmission electron microscopy (TEM) images, HRTEM images, and EDS mapping were obtained by a JEOL JEM2100F TEM with an EX-24063 JGT EDS. The average relative density and porosity of the ceramics were determined using the Archimedes method. The residual stress and phonon anharmonicity in BCTZ- x AlN ceramics were evaluated by a Raman spectroscope (LabRAM HR Evolution, Horiba, France). X-ray photoelectron spectroscopy (XPS) was performed on a photoelectron spectrometer (ESCALAB, 250Xi, Thermo Fisher, USA). Thermogravimetric analysis (TG) and differential scanning calorimetry (DSC) were carried out for BCTZ and BCTZ-1.75AlN-300 powders at a heating rate of $20^\circ\text{C min}^{-1}$ (STA449F5 Jupiter, NETZSCH, Germany). Thermal expansion coefficient of ceramic was measured using a Thermal dilatometer (DIL1412STD, Orton, USA). Switching Spectroscopy Piezoelectric Force Microscope (SS-PFM) and Kelvin probe force microscopy (KPFM) measurements were performed using a Dimension Icon Atomic Force Microscope (Bruker, USA).

Electrical property measurements

For electrical measurements, an Ag electrode ($\sim 0.8\text{ cm}$ in diameter, $\sim 17\text{ }\mu\text{m}$ thick) was screen-printed on the ceramic surface and then fired at 550°C for 30 min. The ceramic disks were polarized in a silicone oil bath at room temperature under a DC field of 4 kV mm^{-1} for 30 min. Quasi-static piezoelectric coefficient (d_{33}) was subsequently quantified using a quasi-static piezoelectric constant meter (ZJ-3A, Institute of Acoustics, China). Planar electromechanical coupling factor (k_p), relative permittivity (ϵ_r), dielectric loss ($\tan\delta$) at 1 kHz, and impedance spectra were determined using a capacitance meter (Agilent 4294 A, Agilent, Santa Clara, USA). Temperature-dependent dielectric properties were measured from -50°C to 200°C (Agilent E4980A, Agilent, Santa Clara, USA). Ferroelectric polarization–electric field hysteresis (P – E) loops and electric strain–electric field (S – E) curves were measured using a ferroelectric analyzer (aixACCT TF Analyzer 3000, Aachen, Germany) with a laser interferometer vibrometer (SP-S120/500, sios Mebtechnik GmbH, Germany) at a frequency of 1 Hz. In-situ d_{33} of ceramics was measured using the high-temperature in-situ piezoelectric tester (TZDM-D33T, Harbin Julang Technology Co. Ltd, China).

Computational methodology

The total energies of the R, O, T, and C phases of bulk BaTiO_3 under different strain conditions were calculated using first-principles simulations within density functional theory (DFT)^{56,57}. The projected augmented wave pseudopotentials method was used as implemented in the Vienna *Ab initio* Simulation Package (VASP)^{58,59}. The exchange correlation energy was calculated using the generalized gradient approximation (GGA) of the Perdew–Burke–Ernzerhof form ref. 60. The plane wave cutoff energy was set to 500 eV. The Monkhorst–Pack k -point mesh was taken as $13 \times 13 \times 13$ ⁶¹. Utilizing the conjugate gradient method, the plane lattice constant and atomic coordinates were fully relaxed until the energy and force converged to 10^{-5} eV and 10^{-2} eV/\AA , respectively.

Reporting summary

Further information on research design is available in Nature Portfolio Reporting Summary linked to this article.

Data availability

The authors declare that the data that support the findings of this study are available within the article and its Supplementary Information files. All other relevant data are available from the corresponding authors upon request.

References

1. Waqar, M., Wu, H., Chen, J., Yao, K. & Wang, J. Evolution from lead-based to lead-free piezoelectrics: engineering of lattices, domains, boundaries, and defects leading to giant response. *Adv. Mater.* **34**, 2106845 (2021).
2. Liu, W. & Ren, X. Large piezoelectric effect in Pb-free ceramics. *Phys. Rev. Lett.* **103**, 257602 (2009).
3. Panda, P. K., Sahoo, B., Thejas, T. S. & Krishna, M. High d_{33} lead-free piezoceramics: a review. *J. Electron. Mater.* **51**, 938–952 (2022).
4. Benabdallah, F. et al. Structure–microstructure–property relationships in lead-free BCTZ piezoceramics processed by conventional sintering and spark plasma sintering. *J. Eur. Ceram. Soc.* **35**, 4153–4161 (2015).
5. Wi, S. W., Seo, J. W., Lee, Y. S. & Chung, J. S. Effects of structural phase changes on the luminescence of Eu-doped $(1-x)\text{BaTiO}_3$ - $x\text{CaZrO}_3$. *Ceram. Int.* **49**, 19766–19772 (2023).
6. Hamza, A. et al. Effect of rare-earth substitution on the electrical properties and Raman spectroscopy of BCTZ ceramics. *J. Alloy. Compd.* **735**, 2523–2531 (2018).
7. Wang, X. et al. Ultra-high piezoelectric performance by rational tuning of heterovalent-ion doping in lead-free piezoelectric ceramics. *Nano Energy* **101**, 107580 (2022).

8. Han, C. et al. High piezoelectric coefficient of Pr_2O_3 -doped $\text{Ba}_{0.85}\text{Ca}_{0.15}\text{Ti}_{0.90}\text{Zr}_{0.10}\text{O}_3$ ceramics. *Ceram. Int.* **38**, 6359–6363 (2012).
9. Tian, Y. et al. Piezoelectricity and thermophysical properties of $\text{Ba}_{0.90}\text{Ca}_{0.10}\text{Ti}_{0.96}\text{Zr}_{0.04}\text{O}_3$ ceramics modified with amphoteric Nd^{3+} and Y^{3+} dopants. *Materials* **16**, 2369 (2023).
10. Yang, Y. et al. Effects of V_2O_5 doping on the structure and electrical properties of BCZT lead-free piezoelectric ceramics. *J. Mater. Sci. Mater. Electron.* **30**, 2854–2863 (2019).
11. Huang, X., Gao, C., Huang, M. & Yue, Z. Influence of Co ion doped amount on property of BCTZ piezoelectric ceramics sintered at low temperature. *Ferroelectrics* **481**, 146–154 (2015).
12. Chao, X., Wang, J., Wei, L., Gou, R. & Yang, Z. Electrical properties and low temperature sintering of BiAlO_3 doped ($\text{Ba}_{0.85}\text{Ca}_{0.15}$) ($\text{Zr}_{0.1}\text{Ti}_{0.9}$) O_3 lead-free piezoelectric ceramics. *J. Mater. Sci. Mater. Electron.* **26**, 7331–7340 (2015).
13. Ma, J. et al. Dielectric, ferroelectric, and piezoelectric properties of Sb_2O_3 -modified ($\text{Ba}_{0.85}\text{Ca}_{0.15}$)($\text{Zr}_{0.1}\text{Ti}_{0.9}$) O_3 lead-free ceramics. *J. Mater. Sci. Mater. Electron.* **25**, 992–996 (2014).
14. Dhole, S., Chen, A., Nie, W., Park, B. & Jia, Q. Strain engineering: a pathway for tunable functionalities of perovskite metal oxide films. *Nanomaterials* **12**, 835 (2022).
15. Schlom, D. G. et al. Strain tuning of ferroelectric thin films. *Annu. Rev. Mater. Res.* **37**, 589–626 (2007).
16. Tang, Y. L., Zhu, Y. L., Liu, Y., Wang, Y. J. & Ma, X. L. Giant linear strain gradient with extremely low elastic energy in a perovskite nanostructure array. *Nat. Commun.* **8**, 15994 (2017).
17. Cui, A. et al. Designing monoclinic heterophase coexistence for the enhanced piezoelectric performance in ternary lead-based relaxor ferroelectrics. *ACS Appl. Mater. Inter.* **14**, 10535–10545 (2022).
18. Haeni, J. H. et al. Room-temperature ferroelectricity in strained SrTiO_3 . *Nature* **430**, 758–761 (2004).
19. Dubourdieu, C. et al. Switching of ferroelectric polarization in epitaxial BaTiO_3 films on silicon without a conducting bottom electrode. *Nat. Nanotechnol.* **8**, 748–754 (2013).
20. Choi, K. J. et al. Enhancement of ferroelectricity in strained BaTiO_3 thin films. *Science* **306**, 1005–1009 (2004).
21. Zhang, N. et al. Symmetry of the underlying lattice in (K, Na) NbO_3 -based relaxor ferroelectrics with large electromechanical response. *ACS Appl. Mater. Inter.* **13**, 7461–7469 (2021).
22. Dong, Y., Zou, K., Liang, R. & Zhou, Z. Review of BiScO_3 - PbTiO_3 piezoelectric materials for high temperature applications: fundamental, progress, and perspective. *Prog. Mater. Sci.* **132**, 101026 (2023).
23. Zheng, T., Wu, J., Xiao, D. & Zhu, J. Recent development in lead-free perovskite piezoelectric bulk materials. *Prog. Mater. Sci.* **98**, 552–624 (2018).
24. Li, P. et al. Ultrahigh piezoelectric properties in textured (K, Na) NbO_3 -based lead-free ceramics. *Adv. Mater.* **30**, 1705171 (2018).
25. Luo, X. et al. Greatly improved piezoelectricity and thermal stability of (Na, Sm) Co-doped $\text{CaBi}_2\text{Nb}_2\text{O}_9$ ceramics. *Adv. Powder Mater.* **2**, 100116 (2023).
26. Zhang, Y. & Li, J.-F. Review of chemical modification on potassium sodium niobate lead-free piezoelectrics. *J. Mater. Chem. C* **7**, 4284–4303 (2019).
27. Liu, W. et al. Ultrahigh piezoelectricity and temperature stability in piezoceramics by synergistic design. *Nat. Commun.* **16**, 1527 (2025).
28. Saito, Y. et al. Lead-free piezoceramics. *Nature* **432**, 84–87 (2004).
29. Wang, D. et al. Composition and temperature dependence of structure and piezoelectricity in $(1-x)(\text{K}_{1-y}\text{Na}_y)\text{NbO}_{3-x}(\text{Bi}_{1/2}\text{Na}_{1/2})\text{ZrO}_3$ lead-free ceramics. *J. Am. Ceram. Soc.* **100**, 627–637 (2016).
30. Wang, D. et al. Temperature-dependent, large electromechanical strain in Nd-doped BiFeO_3 - BaTiO_3 lead-free ceramics. *J. Eur. Ceram. Soc.* **37**, 1857–1860 (2017).
31. Han, J., Yin, J. & Wu, J. BNT-based ferroelectric ceramics: electrical properties modification by Ta_2O_5 oxide addition. *J. Am. Ceram. Soc.* **103**, 412–422 (2019).
32. Liu, Q. et al. High-performance lead-free piezoelectrics with local structural heterogeneity. *Energy Environ. Sci.* **11**, 3531–3539 (2018).
33. Gao, J. et al. Phase transition behaviours near the triple point for Pb-free $(1-x)\text{Ba}(\text{Zr}_{0.2}\text{Ti}_{0.8})\text{O}_3$ - $x(\text{Ba}_{0.7}\text{Ca}_{0.3})\text{TiO}_3$ piezoceramics. *EPL* **115**, 37001 (2016).
34. Yan, X., Zheng, M., Gao, X., Zhu, M. & Hou, Y. High-performance lead-free ferroelectric BZT–BCT and its application in energy fields. *J. Mater. Chem. C* **8**, 13530–13556 (2020).
35. Yotthuan, S. et al. Phase ratio, dielectric, ferroelectric, and magnetic properties of BCTZ ceramics with CuO doping synthesized by the solid state combustion technique. *Phys. Status Solidi A* **216**, 1800803 (2019).
36. Ahmed, T. et al. Effective A-site modulation and crystal phase evolution for high ferro/piezoelectric performance in ABO_3 compounds: yttrium-doped BiFeO_3 - BaTiO_3 . *J. Alloy. Compd.* **933**, 167709 (2023).
37. Le, D. T. et al. Effects of the domain size on local d_{33} in tetragonal $(\text{Na}_{0.53}\text{K}_{0.45}\text{Li}_{0.02})(\text{Nb}_{0.8}\text{Ta}_{0.2})\text{O}_3$ ceramics. *J. Am. Ceram. Soc.* **96**, 174–178 (2012).
38. Zuo, R., Fu, J., Yin, G. Z., Li, X. L. & Jiang, J. Z. Electric field induced phase instability in typical (Na, K)(Nb, Sb) O_3 - LiTaO_3 ceramics near orthorhombic and tetragonal phase boundary. *Appl. Phys. Lett.* **101**, 092906 (2012).
39. Chen, X. et al. Effects of interfacial residual stress on mechanical behavior of SiC_f/SiC composites. *J. Adv. Ceram.* **11**, 94–104 (2021).
40. Farhi, R., ElMarssi, M., Simon, A. & Ravez, J. A Raman and dielectric study of ferroelectric $\text{Ba}(\text{Ti}_{1-x}\text{Zr}_x)\text{O}_3$ ceramics. *Eur. Phys. J. B* **9**, 599–604 (1999).
41. Miao, S. et al. Polar order and diffuse scatter in $\text{Ba}(\text{Ti}_{1-x}\text{Zr}_x)\text{O}_3$ ceramics. *J. Appl. Phys.* **106**, 114111 (2009).
42. D’Ippolito, V., Andreozzi, G. B., Bersani, D. & Lottici, P. P. Raman fingerprint of chromate, aluminate and ferrite spinels. *J. Raman Spectrosc.* **46**, 1255–1264 (2015).
43. Qiao, J., Li, L., Peng, W., Xue, T. & Du, M. The effect of residual stresses and dislocations on microwave dielectric loss in rutile-related $(\text{Ti}_{0.6}\text{Zr}_{0.4})_{0.8}(\text{Zn}_{1/3}\text{Nb}_{2/3})_{0.2}\text{O}_2$. *Ceram. Int.* **48**, 239–247 (2022).
44. Lan, T., Li, C. W. & Fultz, B. Phonon anharmonicity of rutile SnO_2 studied by Raman spectrometry and first principles calculations of the kinematics of phonon-phonon interactions. *Phys. Rev. B* **86**, 134302 (2012).
45. Liu, Y. et al. High-performance electrostrictive relaxors with dispersive endotaxial nanoprecipitations. *Adv. Mater.* **34**, 2204743 (2022).
46. Viola, G. et al. Electric field-induced transformations in bismuth sodium titanate-based materials. *Prog. Mater. Sci.* **122**, 100837 (2021).
47. Yao, F.-Z. et al. Diffused phase transition boosts thermal stability of high-performance lead-free piezoelectrics. *Adv. Funct. Mater.* **26**, 1217–1224 (2016).
48. Wang, W. et al. Electrically switchable polarization in $\text{Bi}_2\text{O}_2\text{Se}$ ferroelectric semiconductors. *Adv. Mater.* **35**, 2210854 (2023).
49. Wang, L. et al. Bandgap engineering of BZT–BCT by Mn doping and the emerging strong photo-pyroelectric effect. *Nano Energy* **119**, 109081 (2024).
50. Farahani, H., Wagiran, R. & Urban, G. A. Barium strontium titanate-based humidity sensors: microstructure, surface morphology, dopant influence, and transduction mechanism investigations. *ACS Appl. Electron. Mater.* **3**, 4919–4933 (2021).
51. Zhang, X. et al. FeO_6 octahedral distortion activates lattice oxygen in perovskite ferrite for methane partial oxidation coupled with CO_2 splitting. *J. Am. Chem. Soc.* **142**, 11540–11549 (2020).

52. Wei, X., Chen, C., Fu, X. Z. & Wang, S. Oxygen vacancies-rich metal oxide for electrocatalytic nitrogen cycle. *Adv. Energy Mater.* **14**, 2303027 (2023).
53. Toby, B. H. EXPGUI, a graphical user interface for GSAS. *J. Appl. Crystallogr.* **34**, 210–213 (2001).
54. Larson A. C. & Dreele R. B. V. General Structure Analysis System (GSAS). Report No. LAUR 86-748 (Los Alamos National Laboratory, 1994).
55. Rietveld, H. M. A profile refinement method for nuclear and magnetic structures. *J. Appl. Crystallogr.* **2**, 65–71 (1969).
56. Kohn, W. & Sham, L. J. Self-consistent equations including exchange and correlation effects. *Phys. Rev.* **140**, A1133–A1138 (1965).
57. Hohenberg, P. & Kohn, W. Inhomogeneous electron gas. *Phys. Rev.* **136**, B864–B871 (1964).
58. Kresse, G. & Hafner, J. Ab initio molecular dynamics for liquid metals. *Phys. Rev. B* **47**, 558–561 (1993).
59. Kresse, G. & Furthmüller, J. Efficient iterative schemes for ab initio total-energy calculations using a plane-wave basis set. *Phys. Rev. B* **54**, 11169–11186 (1996).
60. Perdew, J. P., Burke, K. & Ernzerhof, M. Generalized gradient approximation made simple. *Phys. Rev. Lett.* **77**, 3865–3868 (1996).
61. Monkhorst, H. J. & Pack, J. D. Special points for Brillouin-zone integrations. *Phys. Rev. B* **13**, 5188–5192 (1976).

Acknowledgements

The work was supported by the National Natural Science Foundation of China (Grant Nos. 52072150 and 52372194), Taishan Scholars Program (tsqn202312214), and Shandong Province Key Fundamental Research Program (Grant No. ZR2022ZD39). The authors are grateful for the support from the Australian Synchrotron and thank Dr Wenliang Tan for their help during the experiments at the Australian Synchrotron.

Author contributions

Y.S. carried out the experiments, analyzed the data, and wrote the manuscript. Q.W. carried out the experiments. J.W. conducted the SXRD measurements and analyzed the data. W.S. performed the DFT calculations. Y.L. conducted the KPFM study. Y.H. and Z.C. conceived the idea and provided revisions to the manuscript. Y.H., T.W., and Z.C. supervised the project and guided the research. All authors discussed the results and commented on the manuscript.

Competing interests

The authors declare no competing interests.

Additional information

Supplementary information The online version contains supplementary material available at <https://doi.org/10.1038/s41467-025-59311-2>.

Correspondence and requests for materials should be addressed to Yu Huan, Tao Wei or Zhenxiang Cheng.

Peer review information *Nature Communications* thanks Tauseef Ahmed, Parkpoom Jarupoom, and the other, anonymous, reviewer(s) for their contribution to the peer review of this work. A peer review file is available.

Reprints and permissions information is available at <http://www.nature.com/reprints>

Publisher's note Springer Nature remains neutral with regard to jurisdictional claims in published maps and institutional affiliations.

Open Access This article is licensed under a Creative Commons Attribution-NonCommercial-NoDerivatives 4.0 International License, which permits any non-commercial use, sharing, distribution and reproduction in any medium or format, as long as you give appropriate credit to the original author(s) and the source, provide a link to the Creative Commons licence, and indicate if you modified the licensed material. You do not have permission under this licence to share adapted material derived from this article or parts of it. The images or other third party material in this article are included in the article's Creative Commons licence, unless indicated otherwise in a credit line to the material. If material is not included in the article's Creative Commons licence and your intended use is not permitted by statutory regulation or exceeds the permitted use, you will need to obtain permission directly from the copyright holder. To view a copy of this licence, visit <http://creativecommons.org/licenses/by-nc-nd/4.0/>.

© The Author(s) 2025